Supplementary Materials

Trace elements in abyssal peridotite olivine record melting, thermal evolution, and melt refertilization in the oceanic upper mantle. *Contributions to Mineralogy and Petrology* (https://doi.org/10.1007/s00410-023-02044-6)

Kuan-Yu Lin[1], Jessica Warren[1], Fred A Davis[2]
[1]Department of Earth Sciences, University of Delaware
[2]Department of Earth and Environmental Sciences, University of Minnesota Duluth

Supplementary Material A: Extended methods section

Detailed analytical methodology

Optimal laser settings were chosen by performing power tuning to maximize the signal intensity and minimize the relative standard deviation for olivine and pyroxene. For this tuning, we used natural reference materials of olivine, MongOLSh11-2 (Batanova et al. 2019), and pyroxene, Kilbourne Hole xenolith KH03-4 (Harvey et al. 2012). A spot size of 85 μm was selected based on leveraging the analyzable area of olivine grains in our samples alongside sensitivity and uncertainty. Based on our power tuning at this spot size, counts were maximized at a laser repetition rate of 10 Hz and laser set point of 6 mJ with 90% attenuation (fluency = 11 J/cm^2), and 400 shot counts, which corresponds to 40 s ablation time. For pyroxenes, optimized laser settings were obtained with a 110 μm spot size, repetition rate of 8 Hz and laser set point of 7 mJ at 90% attenuation (fluency = 12.37 J/cm^2). We operated the iCAP ICPMS using the kinetic energy discrimination (KED) mode to eliminate cell-formed polyatomic interferences (Yamada 2015). At the beginning of each session, tuning was done on the synthetic glass NIST612 to maximize sensitivity using ^{238}U, ^{232}Th, and ^{139}La while maintaining low elemental fractionation by monitoring ^{238}U/^{232}Th<1.1.

For olivine, we measured the isotopes ^{26}Mg, ^{27}Al, ^{29}Si, ^{44}Ca, ^{48}Ti, ^{51}V, ^{53}Cr, ^{55}Mn, ^{57}Fe, ^{59}Co, ^{60}Ni, ^{66}Zn, ^{89}Y, and ^{172}Yb, with ^{26}Mg as the internal standard. Our list of elements is slightly different from those of De Hoog et al. (2010) for various reasons: The light elements ^{7}Li and ^{23}Na are not measurable under KED mode. Signals of ^{93}Nb and ^{90}Zr were too low for precise quantification. Instead, for Group III elements we added ^{172}Yb because of its similar behavior with ^{89}Y and higher abundance compared to Nb and Zr. We excluded elements including ^{45}Sc and ^{66}Cu to allow more counting time for elements that are of low abundance but of more interest to this study, such as Al, Y, and Yb.

For pyroxenes, we measured the isotopes ^{26}Mg, ^{27}Al, ^{29}Si, ^{44}Ca, ^{48}Ti, ^{51}V, ^{53}Cr, ^{55}Mn, ^{57}Fe, ^{59}Co, ^{60}Ni, ^{63}Cu, ^{66}Zn, ^{85}Rb, ^{88}Sr, ^{89}Y, ^{90}Zr, ^{93}Nb, ^{137}Ba, ^{139}La, ^{140}Ce, ^{141}Pr, ^{146}Nd, ^{147}Sm, ^{151}Eu, ^{159}Tb, ^{160}Gd, ^{163}Dy, ^{165}Ho, ^{166}Er, ^{169}Tm, ^{172}Yb, ^{175}Lu, ^{178}Hf, ^{208}Pb, and ^{232}Th, with ^{26}Mg as the internal standard.

For olivine and pyroxene, dwell times were set to 0.05 s for ^{26}Mg, ^{29}Si, ^{52}Cr, ^{55}Mn, ^{57}Fe, ^{59}Co, ^{60}Ni, ^{66}Zn, 0.1s for ^{51}V, and 0.5 s for all other elements to improve counting statistics at lower

concentrations. Background signals were collected for approximately 8 s ahead of each ablation. The signal for each element during ablation was carefully checked. Cycles with time-resolved signals indicative of spinel inclusions (anomalous spikes of Al, Cr, V) or penetration into a different grain (sudden increase/decrease of signal) were removed (Figure S1), as discussed further below.

Element concentrations were calculated from measured signals in counts per second using working curves constructed by measuring MPI-DING reference glasses GOR-132G, StHs6/80G, KL2-G, T1-G, ML3B-G, ATHO-G (Jochum et al. 2000) and USGS basaltic glasses BHVO-2G, BCR-2G, and BIR-1G (Jochum et al. 2005). We use reference material values from the GeoReM database (Jochum et al. 2005a, 2016; summarized in Table S7). We demonstrate in the Supplementary Material B that matrix-dependent elemental fractionation is insignificant (<10%) at our operating conditions, which is supported by the long-term reproducibility of MongOLSh11-2 in our study (Table S8).

Monitoring spinel inclusions in olivine during LA-ICPMS analysis:

For each laser ablation analysis, the time-resolved ablation signal for each element was carefully checked to ensure the quality of the data. For olivine, we occasionally observed anomalously high Al signals, often coupled with high V and Cr (Fig. S1). Since all other elements in the same ablation spot were unaffected, these high Al, V, and Cr spikes are best explained as contributions from spinel. The large plateaus observed in Fig. S1a suggest ablation into a neighboring spinel grain beneath the olivine grain, whereas the disseminated spikes in Fig. S1 are inclusions of spinel in olivine. This can be easily overlooked if Al, V, Cr are not included when evaluating the data and will yield erratic or anomalously high abundances of these elements.

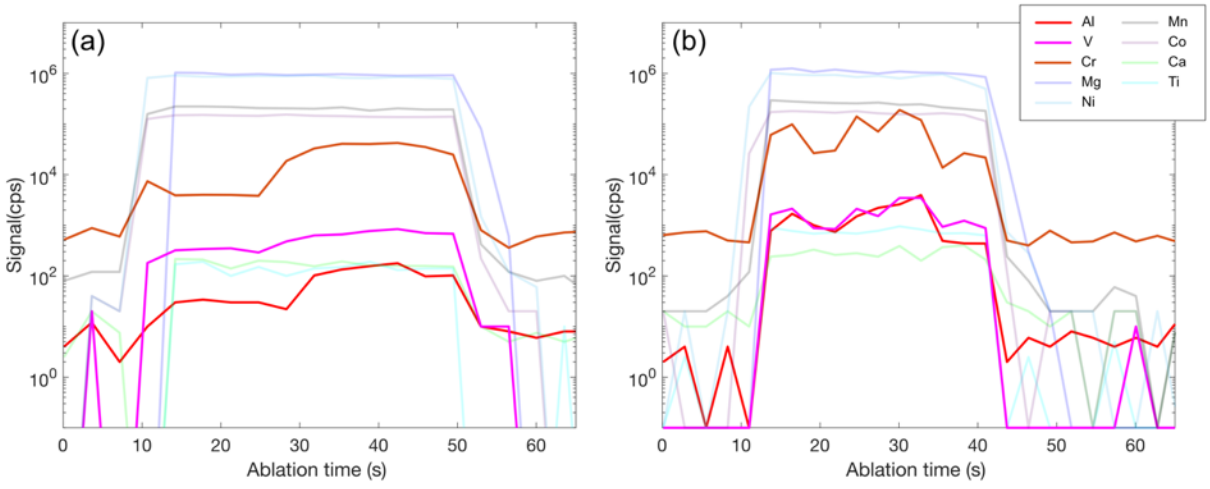

Figure S1 (Supplementary Material A). Time-resolved analyte signal in counts per second (cps) during LA-ICPMS analysis. (a) An example analysis that displays coupled increases in signal intensities for Al, V, and Cr during the latter part of the ablation. We interpret this as ablation into a spinel inclusion. (b) A similar example, but with abundant, smaller spinel inclusions identified by individual peaks of Al, Cr, and V. All other analytes (Mg, Ni, Mn, Co, Ca, and Ti) remained constant throughout the course of ablation.

We found that Al, V, and Cr are often – but not always – coupled, as we identified individual peaks in only two of these three elements during our data analysis. An example can be seen at the very end of the ablation signal in Fig. S1b, where only small spikes of Cr and V are present. Similar spikes for Ca and Ti also occur occasionally, though less ubiquitously compared to Al, V, and Cr. Penetration into other mineral grains such as pyroxene, serpentine, or epoxy in some cases can also be characterized by sharp increases or decreases of elements specific to these phases. We thus carefully monitored the time-resolved signals when analyzing olivine data to avoid erratic results.

Supplementary Material B: Evaluating matrix effects for the trace element calibration

In LA-ICPMS, the term "matrix effects" refers to inter-elemental fractionations that can occur as a function of the material composition (or "matrix"). Matrix-dependent fractionation can occur throughout the entire instrumental process, including but not limited to: non-stoichiometric ablation at the laser pit, fractionation during transportation, and incomplete ionization in the plasma (Sylvester 2008; Gaboardi and Humayun 2009; Czas et al. 2012). These effects can compromise the derivation of absolute abundances from LA-ICPMS data (e.g., Jackson, 2008).

The calibration of laser data assumes that the ratio of sensitivity (defined here as counts per second (cps) per concentration, or cps/ppm) of the analyte isotope over the internal standard (i.e., a coexisting element in the material that has been independently characterized of concentration) is the same between the sample and the calibration standard(s):

$$\left[\frac{\left(\frac{I}{C}\right)_i}{\left(\frac{I}{C}\right)_{IS}}\right]_{Sample} = \left[\frac{\left(\frac{I}{C}\right)_i}{\left(\frac{I}{C}\right)_{IS}}\right]_{CS} \quad \text{(S1)}$$

where I is intensity (in cps), C stands for concentration (in ppm), $\left(\frac{I}{C}\right)_i$ is the sensitivity of the analyte i, IS stands for internal standard, and CS stands for the calibration standard. The term $[C_i]_{sample}$ is the concentration of the target analyte to be determined, while the other terms are either measured or previously constrained. Matrix-dependent fractionations can invalidate the assumption of Equation S1, producing biased values. Hence, the analyte/IS sensitivity ratios between the sample and reference materials were checked to confirm reasonable similarity during LA-ICPMS analysis.

The most straightforward way to evaluate similarity between sample and reference materials is to calculate the slope on a working curve (Fig. S2). Working curves were constructed by measuring a set of reference materials of known concentration to establish the correlation between analyte signal and absolute concentration. For analyses that incorporate an internal standard (I_{IS}), the normalized cps (I_i/I_{IS}) multiplied by the concentration of the internal standard (C_{IS}) is plotted on the y-axis against the accepted concentration of element i on the x-axis. The slope (m) of this curve is the sensitivity ratio between the target analyte and the internal standard (which is also the right-hand side of Equation S1):

$$m = \frac{\frac{I_i}{I_{IS}} \times C_{IS}}{C_i} = \frac{\frac{I_i}{C_i}}{\frac{I_{IS}}{C_{IS}}} = \frac{S_i}{S_{IS}} \quad \text{(S2)}$$

where S is the sensitivity (cps/ppm).

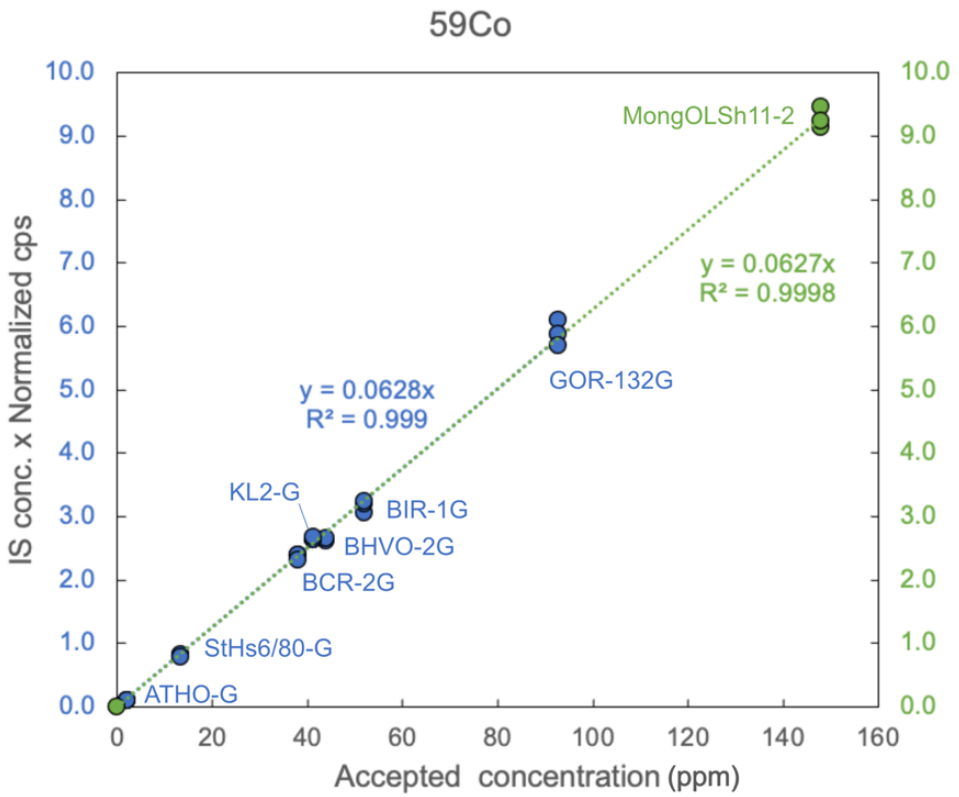

Figure S2 (Supplementary Materials B). Working curve example for $^{59}Co/^{26}Mg$ (where ^{26}Mg is used as the internal standard). The blue circles are analyses of MPI-DING and USGS standards, which are regressed and forced through the origin to construct a working curve (regression results shown in blue). Three spots were measured for each standard. The green dots are analyses of the olivine reference material MongOLSh11-2 (Batanova et al. 2019), with a working curve calculated assuming the lines passes through the origin (green dotted line). The difference in slopes between the multi-standard (0.0628) and olivine (0.0627) working curves is minimal. This suggests that no significant matrix effect occurred and that the glass working curve can be used to calibrate olivine.

If the working curve of an element determined from a matrix-matched reference material has the same slope as one determined from a reference material of a different matrix, this suggests no matrix effects between the two types of materials. Only one standard is available for olivine analysis by LA-ICPMS, whereas many basaltic and andesitic glasses have been characterized as reference materials (e.g., Jochum et al., 2016). Hence, if no matrix effect occurs between these glasses and olivine, then Equation S1 is assumed to be valid, and olivine can be calibrated using glass reference materials.

Batanova et al. (2019) provided an olivine reference material, MongOLSh11-2, that we tested against glass reference materials for matrix effects. As demonstrated by the example in Fig. S2 of ^{59}Co (with ^{26}Mg as the internal standard), the multi-standard working curve based on basalt glasses has a near-identical slope to that of MongOLSh11-2 olivine. This indicates the equivalence of the matrix-matched and multi-standard calibration, which we confirmed for all elements in this study. We then used the glass reference materials for calibration, given the limited amount of

MongOLSh11-2 available. This also allowed us to use this olivine as a secondary reference material to evaluate long-term reproducibility and data quality (Table S8).

Supplementary Material C. Assessing core-rim compositional variation in abyssal peridotite olivine.

To evaluate the extent of compositional zoning in olivine, we selected a peridotite from the Gakkel ridge (PS59-235-17, residual lherzolite) and performed core-rim analyses on six olivine grains using LA-ICPMS. The methodology is the same as outlined in Section 4 of the main text and the data is compiled in Table S9.

A representative profile of a 2-3 mm size olivine grain is shown in Fig. S3. Among the five analyzed profiles, major elements (Mg and Si) have flat profiles with no zonation, as are most divalent transitional metal cations including Mn, Co, Ni, and Zn (not shown). For Ca, around half of the surveyed grains display core-rim variability, but the pattern does not resemble a diffusion profile (Fig. S3a). Three elements – Ti, V, and Cr – often show core-rim zoning (Figs. S3b and c). Core-rim transects of Al have random variations across the grain with no identifiable core-rim zonation (Fig. S3c). Y and Yb are not zoned in most of the profiles (Fig. S3d), but occasionally show either reverse or normal zoning patterns that within approximately 200 μm of the rim.

For each element, sample versus grain averages and one standard deviations are plotted in Fig. S3. All the elements in this grain have average and one standard deviations indistinguishable from the sample average. The grain average for Al and Ti is slightly lower than the sample average, but within uncertainty. This implies that the sample averages and standard deviations reported in this study, which are calculated from measurements on apparent "cores", represent the extent of compositional variability within the sample. For more serpentinized samples, measuring the center of available olivine relicts might in fact be sampling different parts of the grain, in which case the sample average and standard deviation should thus be representative of the rock composition and variability, similar to the example shown here.

Though Ti, V, and Cr are not discussed in detail in this study, the existence of core-rim zonation can potentially be useful for future studies that investigate cooling-induced diffusion profiles in olivine to extract cooling rates/timescales of olivine-bearing plutonic rocks (e.g., Ferrando et al. 2020). So far the diffusivity of Ti and Cr in olivine have been experimentally determined (Ito and Ganguly 2006; Cherniak and Liang 2014; Jollands et al. 2018), but not that of V.

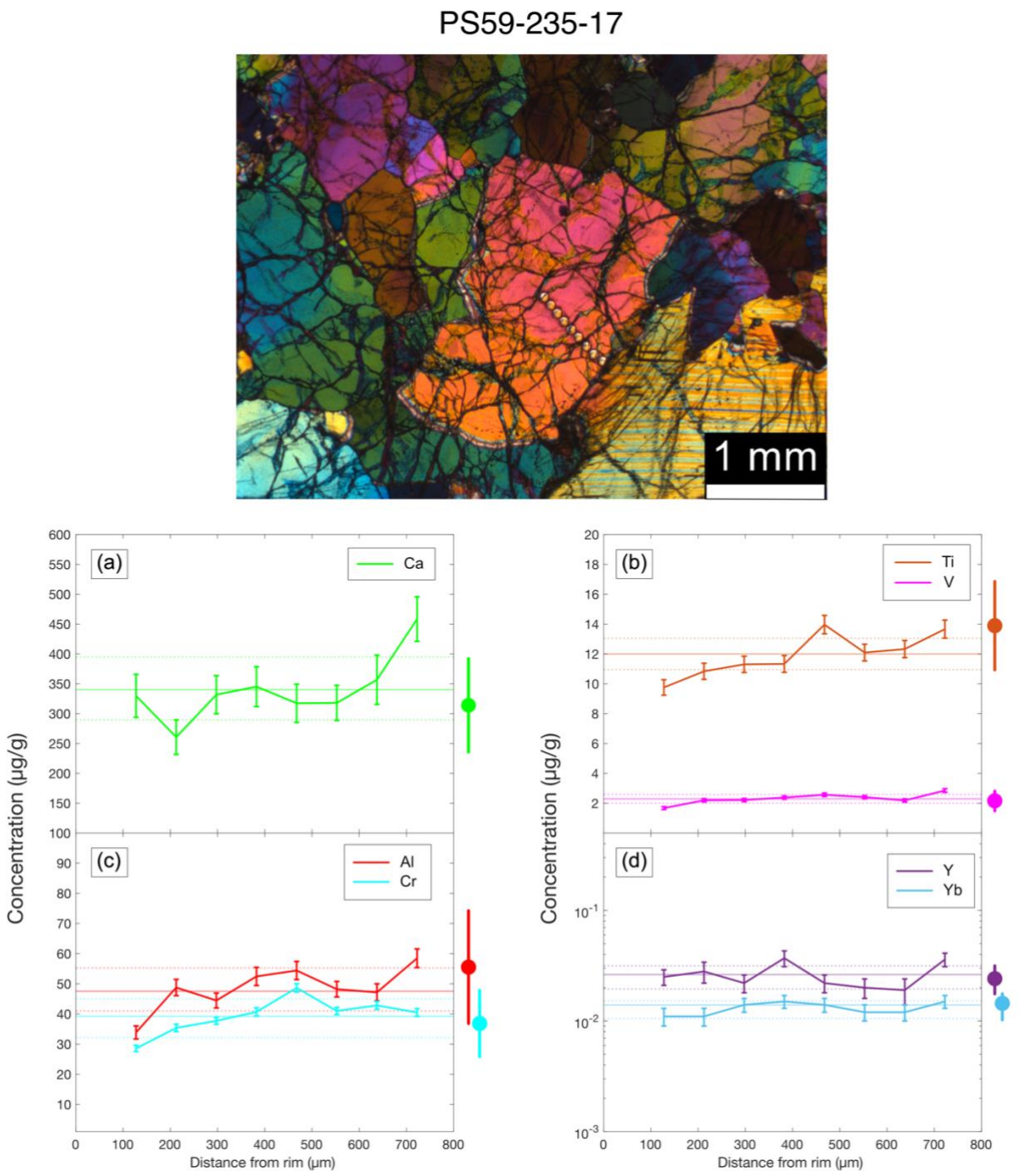

Figure S3 (Supplementary Material C). Photomicrograph in cross-polarized light of a representative rim-to-core concentration transect in an olivine grain in relatively fresh sample PS59-235-17. Each dot on the grain represents a laser pit of 85µm diameter. (a)-(d) Concentration and one standard deviation of elements Ca, Ti, V, Al, Cr, Y, and Yb plotted against distance from rim. The average and one standard deviation of this grain are plotted in solid and dashed lines, respectively, color coded for different elements. The average and one standard deviation for all core analyses of olivine from this sample (Table S1) is plotted to the right of the panels. Data of each spot is summarized in Table S9.

Supplementary Material D: Co-variation between Group I elements.

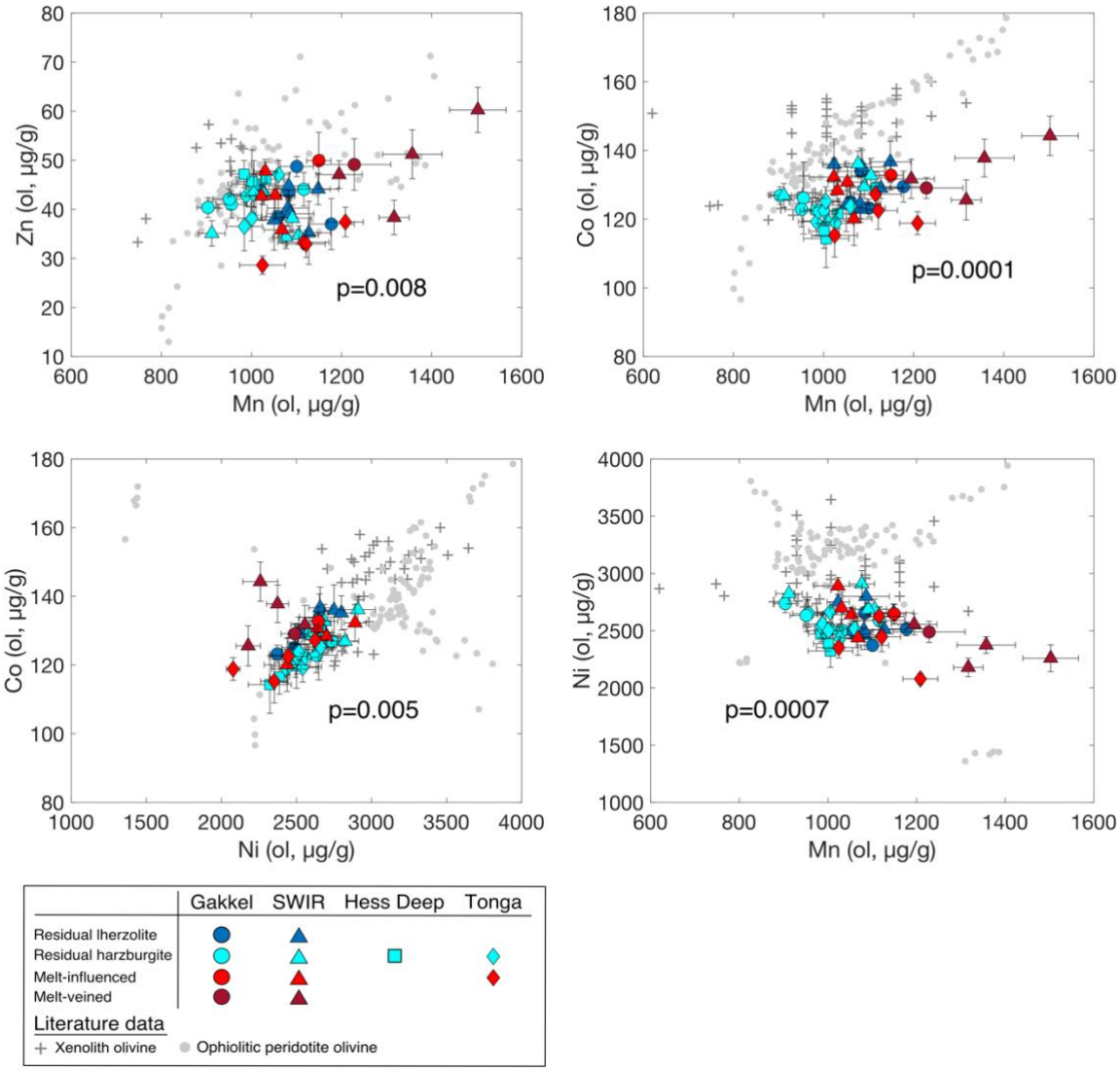

Figure S4 (Supplementary Materials D). Co-variation between Group I elements. P-values obtained using Pearson statistics and two-tailed t-test. All elements are significantly correlated with a p-value threshold of 0.05.

Supplementary Material E: Evaluating the effect of spinel Cr# on $T_{Al}^{ol\text{-}spl}$

To evaluate the effect of spinel Cr# on $T_{Al}^{ol\text{-}spl}$, we first plot the isotherms in spinel Cr# versus the olivine/spinel Al_2O_3 ratio according to the $T_{Al\text{-}in\text{-}ol}$ calibration by Wan et al. (2008), see Fig. S5 below. To simulate the effect of spinel Cr# continuing to change on $T_{Al\text{-}in\text{-}ol}$ during cooling, we ran a simple model with a random starting sample (Kn162-9-50-7), highlighted with a red box in the figure. We assume that the Al_2O_3 in olivine remains constant, and that Al is added to spinel while the same amount of Cr is removed from spinel during cooling, so that spinel Cr# decreases while total Cr+Al remains constant, and the olivine/spinel Al_2O_3 ratio decreases. This results in a decrease of spinel Cr#, which is in agreement with the model of Voigt and von der Handt (2011). The results are plotted on the diagram below in blue asterisks and lie parallel to the isotherms (each asterisk depicts 0.01 mol of Al addition/Cr removal). This indicates that spinel Cr# variation during cooling probably has little effect on the observed $T_{Al\text{-}in\text{-}ol}$. Therefore, the lower values for $T_{Al\text{-}in\text{-}ol}$ compared to $T_{Ca\text{-}in\text{-}ol}$ is more likely due to faster diffusivity of Al in olivine, as suggested in the text.

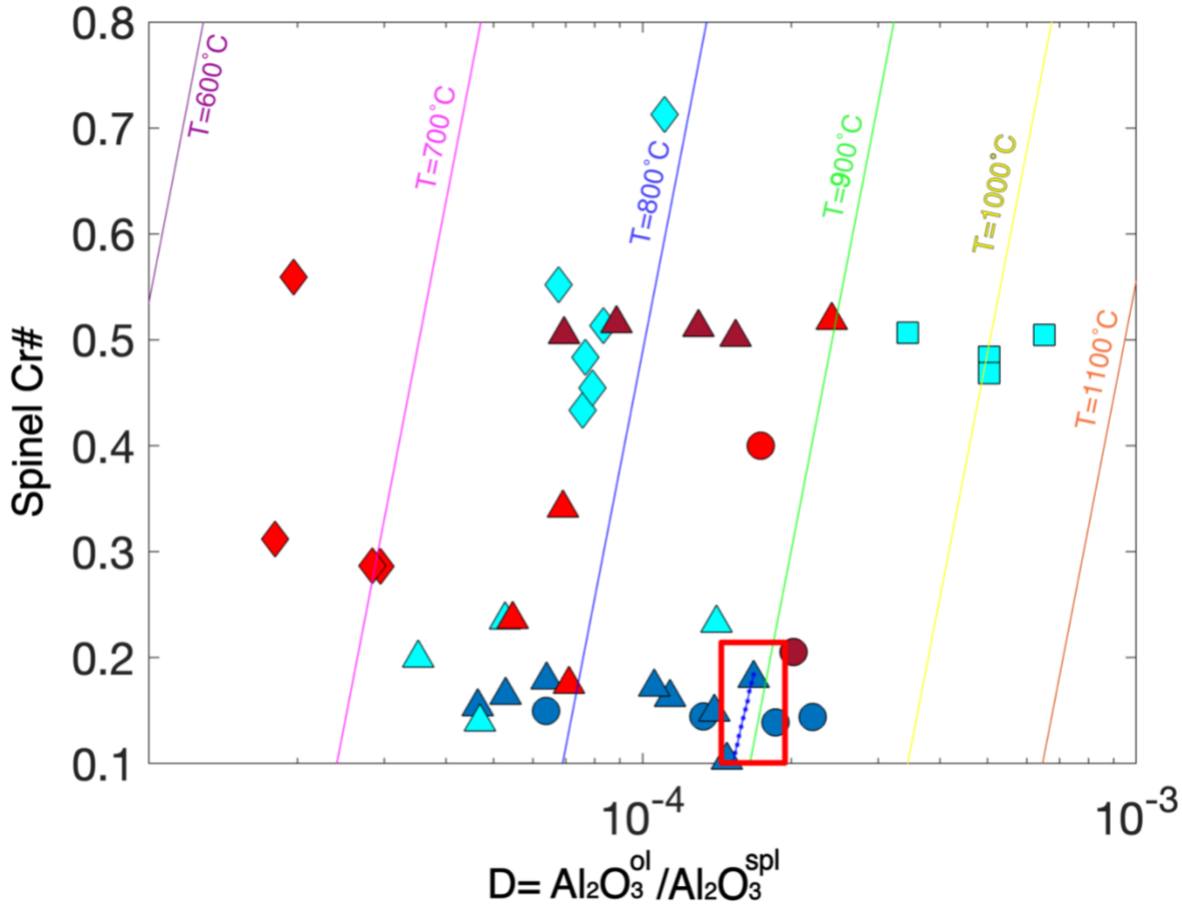

Figure S5 (Supplementary Materials E). Plot of spinel Cr# against the ratio of Al_2O_3 (wt%) between olivine and spinel, with experimentally calibrated isotherms from Wan et al. (2008) plotted in different colors. Our model for sample Kn162-9-50-7 is highlighted in the red box (see text above for details).

Supplementary Material F: Additional details of the two-stage model

Mineral/melt partition coefficients (i.e., $D^i_{A/melt}$ where A stands for olivine, cpx, opx, and i denotes Yb and Y) are used in the "Partial melting and sub-solidus redistribution: Ti, Y, and Yb" section. for both the DMM partial melting model and the subsolidus re-equilibration model. Partition coefficients can be temperature, pressure, and composition dependent, and such dependence can be quantified using experimentally calibrated lattice strain models (Sun 2018). We calculated these $D^i_{A/melt}$ values using formulation compiled in Appendix A of Sun and Liang (2014) with the Microsoft Excel spreadsheets with macros provided by C.G. Sun: https://earth-sun.weebly.com/tools.html. For these calculations, the following values were used:

Table S10. Modeling parameters used in Section "Partial melting and sub-solidus redistribution: Ti, Y, and Yb".

	$D^i_{ol/melt}$	$D^i_{opx/melt}$	$D^i_{cpx/melt}$
	Olivine composition	Opx composition	Cpx composition
SiO_2	40.7	53.36	50.61
TiO_2		0.16	0.63
Al_2O_3	0.12[a]	6.46	7.87
Cr_2O_3		0.76	1.2
FeO^T	10.16	6.27	2.94
MnO	0.14	0.12	0.09
MgO	48.59	30.55	16.19
CaO	0.05	2.18	19.52
Na_2O		0.05	0.89
Additional parameters	P=1.5GPa	Melt TiO_2=1.68[b]	Melt H_2O=0.30[c]

Mineral compositions (in wt%) used are from Workman and Hart (2005). For the DMM melting model, we applied T=1350˚C. For subsolidus re-equilibration model, $D^i_{A/melt}$ values were calculated at 1200˚C, 1100˚C, 1000˚C, and 900˚C.

[a]Estimated by using cpx Al_2O_3 from Workman and Hart (2005) and $D^{Al}_{ol/melt}$ and $D^{Al}_{cpx/melt}$ from Laubier et al. (2014)
[b]ALL MORB Mean value from Gale et al. (2013)
[c]Global MORB average from Le Voyer et al. (2019)

Additional details for the two-stage model:

1. The model is extrapolated to 800˚C, which is beyond the temperature range (1190-1470˚C) of the partitioning experiments (Sun and Liang, 2014). Such experiments are difficult at lower temperatures as the time required for multiple phases to equilibrate is too long. One way to evaluate the error of this extrapolation is to apply our model to well-equilibrated

peridotite xenoliths and compare the effectiveness of the models at predicting the observed $D^i_{A/B}$ values, where A and B are coexisting mantle phases and i denotes the element of interest. Sun and Liang (2014) validated this by demonstrating good agreement between the predicted results of their model and the measured values for well equilibrated continental xenoliths (Witt-Eickschen and O'Neill, 2005; Witt-Eickschen et al., 2009).

2. Diffusive exchange between cpx and opx ceases at 1200˚C in our model, with the assumption that Yb and Y values in both pyroxenes remain constant at lower temperatures. Previous studies (Dygert et al., 2017 and references therein) argued that exchange of Y and Yb between pyroxenes ceases within the temperature range 1100-1300˚C based on the T_{REE} values. This assumption means that while $D^i_{ol/melt}$, $D^i_{opx/melt}$ and $D^i_{cpx/melt}$ continue to vary as a function of temperature for T<1200˚C, a kinetic barrier regarding REE exchange between the cpx and opx is imposed. At this stage, only Yb and Y in olivine is still diffusing and redistributing according to $D^i_{cpx/ol}$ and $D^i_{opx/ol}$ at the given temperature. This agrees with the faster diffusivity of these elements in olivine compared to pyroxenes (Fig.8).
3. Our model does not account for the effects of mineral chemistry variations and subsolidus reactions, such as pyroxene exsolution, on subsolidus re-equilibration of major components during cooling. Pyroxene exsolution is ubiquitous throughout the course of peridotite cooling and thus pyroxene modal proportions change. Thermodynamic modeling by Yao (2015) on the effect of modal abundances on REE subsolidus reequilibration demonstrated that modal variations slightly counters the effect of temperature on the redistribution of Yb and Y. The incorporation of these elements into cpx is decreased when compared to models that only account for temperature effects. Thus, considering mass balance and the existence of subsolidus reactions between minerals in natural samples, the extent of Yb and Y loss in olivine during cooling may be slightly less than calculated by our model.

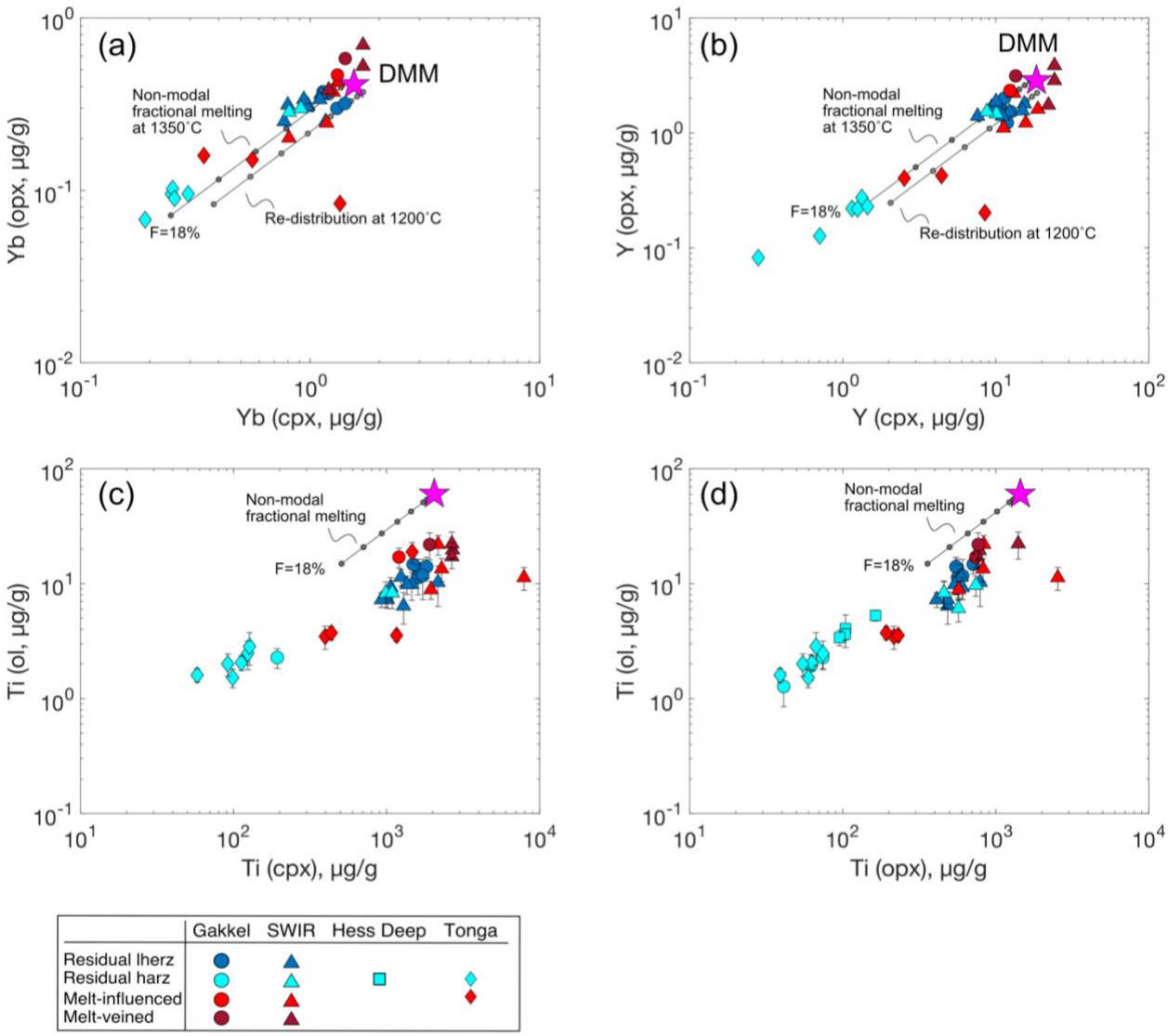

Figure S6 (Supplementary Material F). Results of the melting and re-equilibration model for Yb, Y, and Ti in abyssal peridotite minerals. Non-modal fractional melting model between opx and cpx for Yb (a) and Y (b). A follow-up stage of subsolidus cooling down to 1200˚C is also plotted. Non-modal fractional melting model for Ti in olivine against Ti in cpx (c) and opx (d). Subsolidus redistribution is not modeled for Ti as temperature-dependent partition coefficient models are not available.

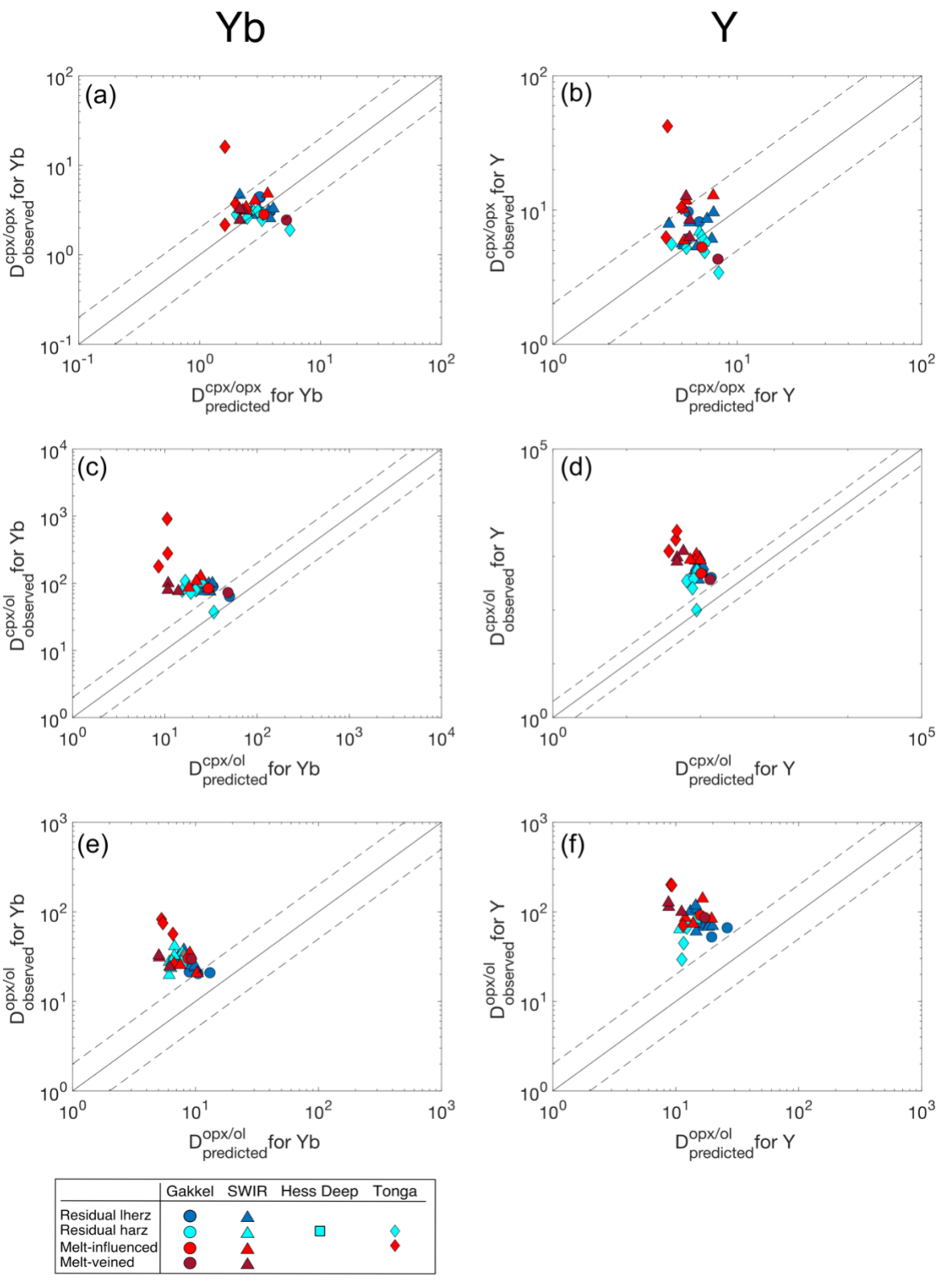
Yb
Y
(a)
(b)
(c)
(d)
(e)
(f)
$D^{cpx/opx}_{observed}$ for Yb
$D^{cpx/opx}_{predicted}$ for Yb
$D^{cpx/opx}_{observed}$ for Y
$D^{cpx/opx}_{predicted}$ for Y
$D^{cpx/ol}_{observed}$ for Yb
$D^{cpx/ol}_{predicted}$ for Yb
$D^{cpx/ol}_{observed}$ for Y
$D^{cpx/ol}_{predicted}$ for Y
$D^{opx/ol}_{observed}$ for Yb
$D^{opx/ol}_{predicted}$ for Yb
$D^{opx/ol}_{observed}$ for Y
$D^{opx/ol}_{predicted}$ for Y
Gakkel
SWIR
Hess Deep
Tonga
Residual lherz
Residual harz
Melt-influenced
Melt-veined

Figure S7. Observed and predicted partitioning values of $D^{i}_{cpx/opx}$ for Yb (a) and Y (b). Observed and predicted partitioning values of $D^{i}_{cpx/ol}$ for Yb (c) and Y (d). Observed and predicted partitioning values of $D^{i}_{opx/ol}$ for Yb (e) and Y (f). Solid lines are 1:1 correspondence lines and dashed lines are 1:2 and 2:1 lines.

Regression plots for T_{REE} values summarized in Table 2 and discussed in Section "Evaluating olivine trace element thermometry".

Residual peridotites

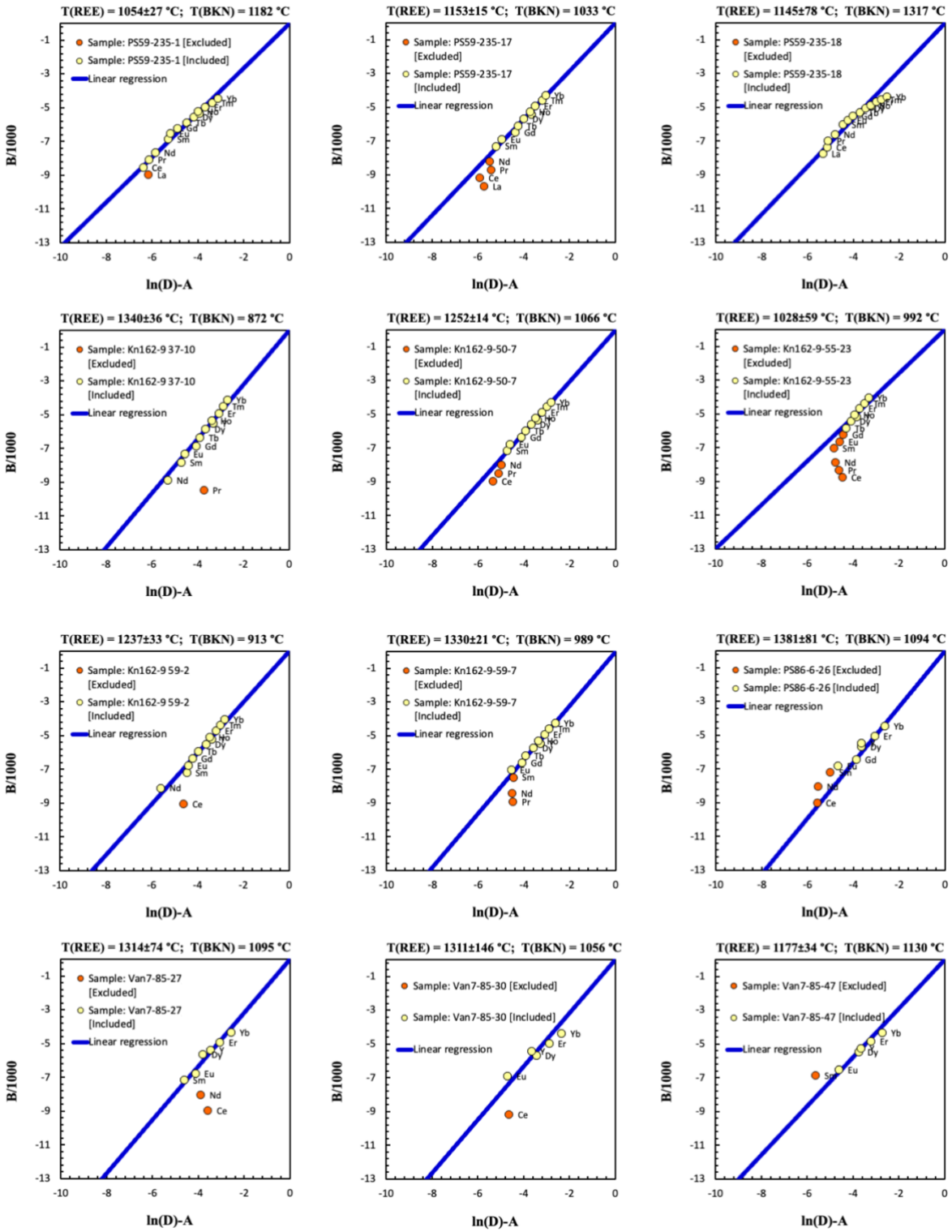

Residual peridotites (continued)

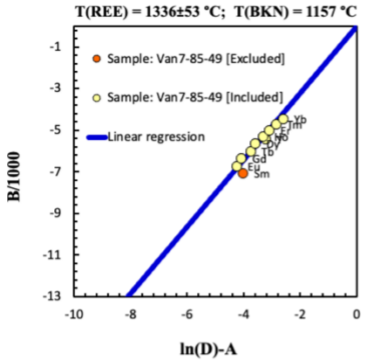

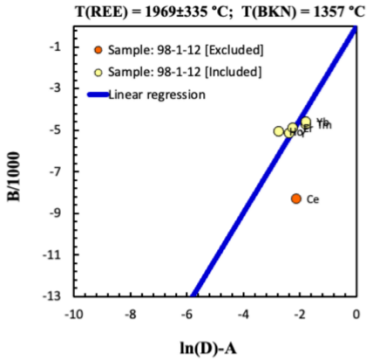

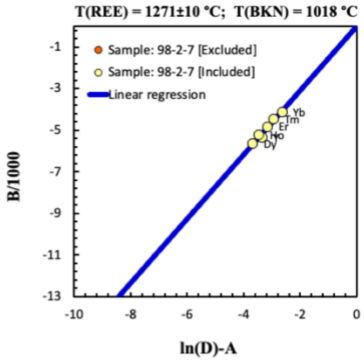

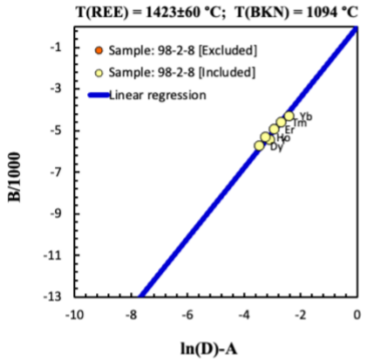

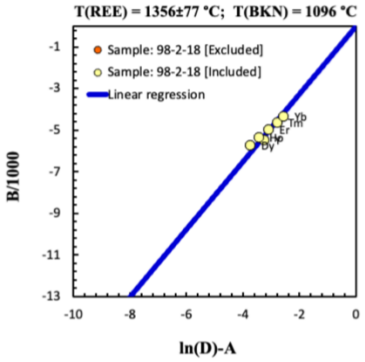

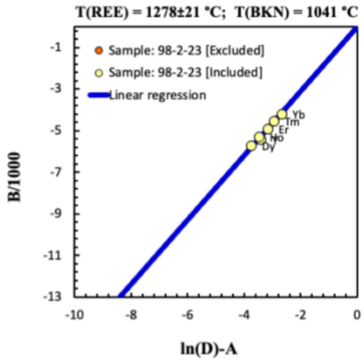

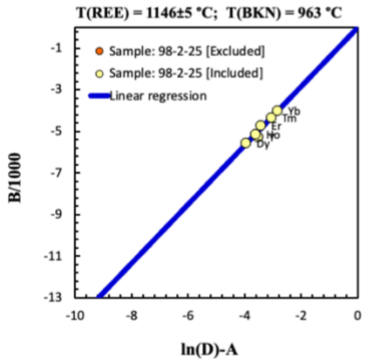

Melt-influenced peridotites

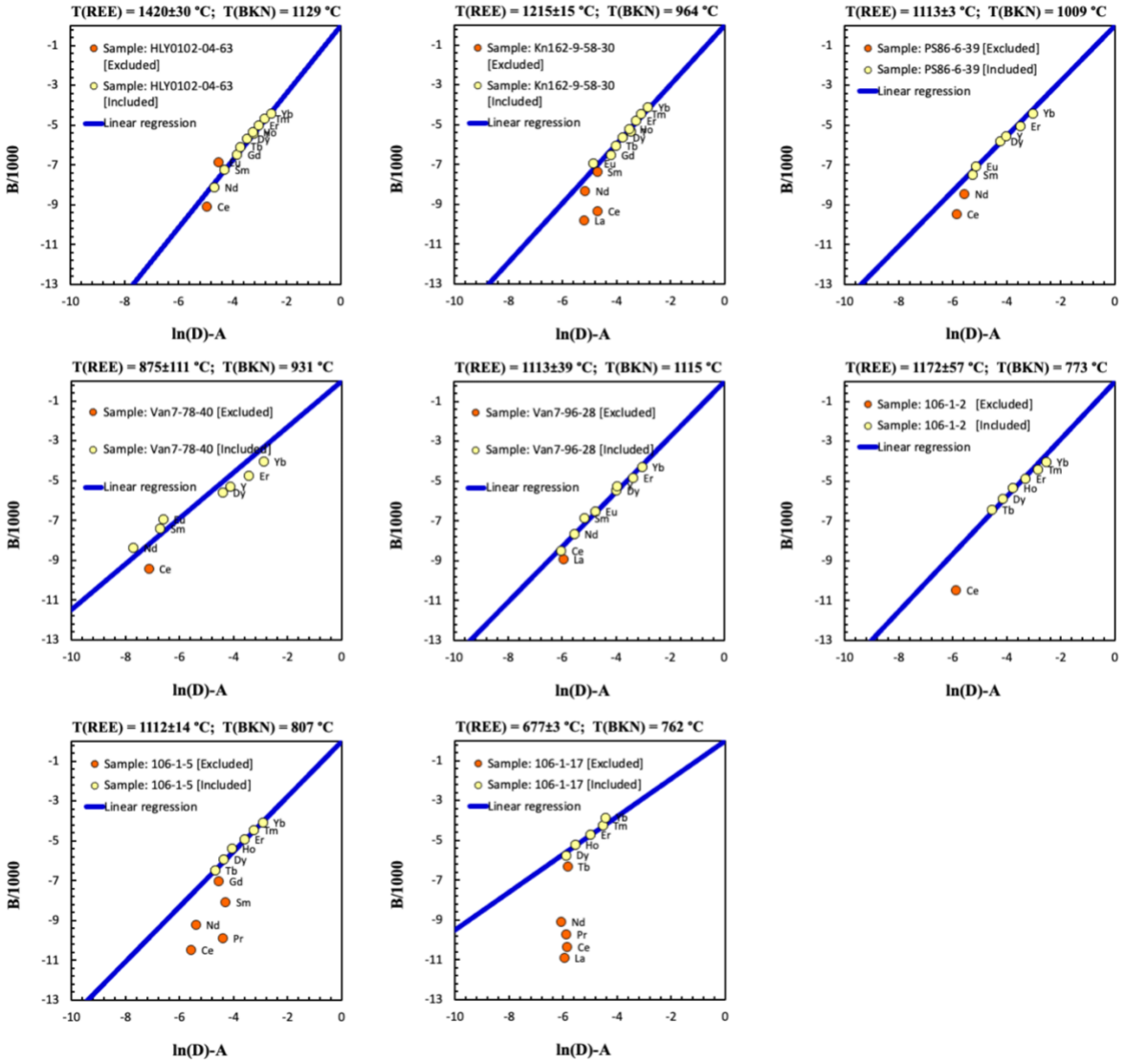

Melt-veined peridotites

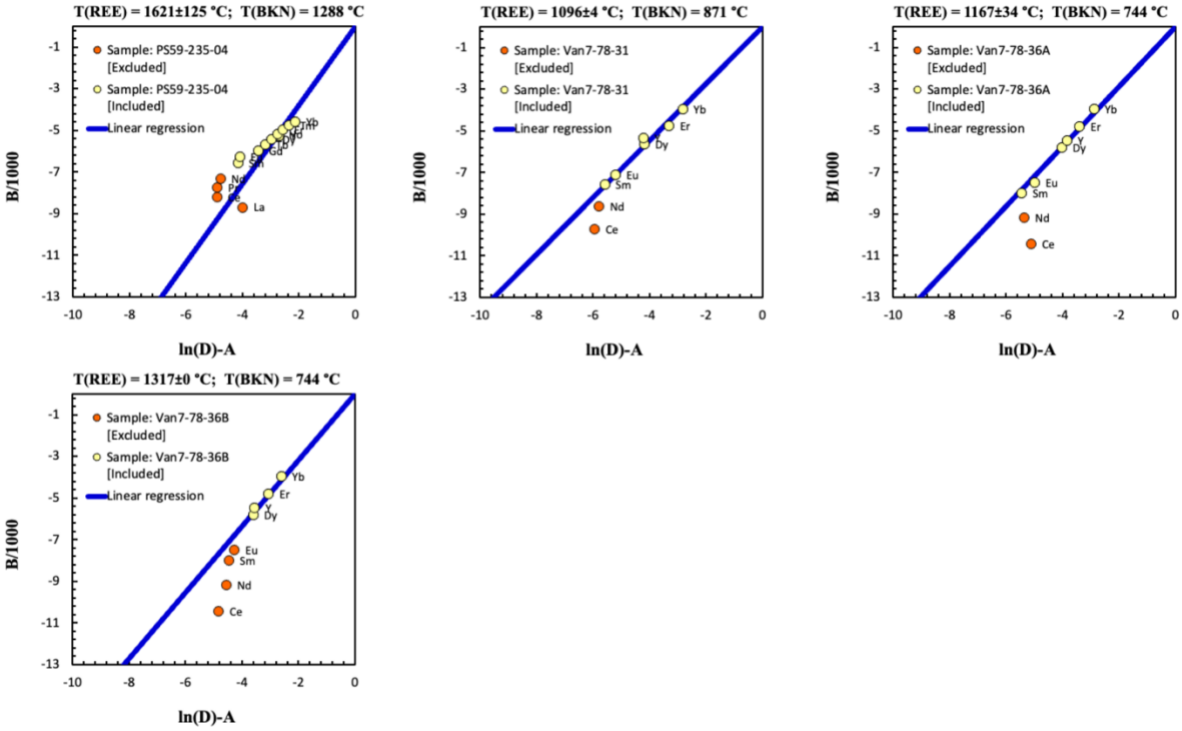

References cited

Batanova VG, Thompson JM, Danyushevsky LV, et al (2019) New olivine reference material for in situ microanalysis. Geostand Geoanal Res 43:453–473. https://doi.org/10.1111/ggr.12266

Cherniak DJ, Liang Y (2014) Titanium diffusion in olivine. Geochimica et Cosmochimica Acta 147:43–57. https://doi.org/10.1016/j.gca.2014.10.016

Czas J, Jochum KP, Stoll B, et al (2012) Investigation of matrix effects in 193nm laser ablation-inductively coupled plasma-mass spectrometry analysis using reference glasses of different transparencies. Spectrochimica Acta Part B: Atomic Spectroscopy 78:20–28. https://doi.org/10.1016/j.sab.2012.09.004

De Hoog JCM, Gall L, Cornell DH (2010) Trace-element geochemistry of mantle olivine and application to mantle petrogenesis and geothermobarometry. Chemical Geology 270:196–215. https://doi.org/10.1016/j.chemgeo.2009.11.017

Dygert N, Kelemen PB, Liang Y (2017) Spatial variations in cooling rate in the mantle section of the Samail ophiolite in Oman: Implications for formation of lithosphere at mid-ocean ridges. Earth and Planetary Science Letters 465:134–144. https://doi.org/10.1016/j.epsl.2017.02.038

Ferrando C, Lynn KJ, Basch V, et al (2020) Retrieving timescales of oceanic crustal evolution at Oceanic Core Complexes: Insights from diffusion modelling of geochemical profiles in olivine. Lithos 376–377:105727. https://doi.org/10.1016/j.lithos.2020.105727

Gaboardi M, Humayun M (2009) Elemental fractionation during LA-ICP-MS analysis of silicate glasses: implications for matrix-independent standardization. J Anal At Spectrom 24:1188. https://doi.org/10.1039/b900876d

Gale A, Dalton CA, Langmuir CH, et al (2013) The mean composition of ocean ridge basalts. Geochem Geophys Geosyst 14:489–518. https://doi.org/10.1029/2012GC004334

Harvey J, Yoshikawa M, Hammond SJ, Burton KW (2012) Deciphering the trace element characteristics in Kilbourne Hole peridotite xenoliths: melt–rock Interaction and metasomatism beneath the Rio Grande Rift, SW USA. Journal of Petrology 53:1709–1742. https://doi.org/10.1093/petrology/egs030

Ito M, Ganguly J (2006) Diffusion kinetics of Cr in olivine and 53Mn–53Cr thermochronology of early solar system objects. Geochimica et Cosmochimica Acta 70:799–809. https://doi.org/10.1016/j.gca.2005.09.020

Jackson SE (2008) Calibration strategies for elemental analysis by la-icp-ms. In: Laser ablation–icp–ms in the earth sciences current practices and outstanding issues. Mineralogical Association of Canada Short Course Series, p 20

Jochum KP, Dingwell DB, Rocholl A, et al (2000) The preparation and preliminary characterisation of eight geological MPI-DING reference glasses for in-situ microanalysis. Geostandards and Geoanalytical Research 24:87–133. https://doi.org/10.1111/j.1751-908X.2000.tb00590.x

Jochum KP, Nohl U, Herwig K, et al (2005a) Georem: a new geochemical database for reference materials and isotopic standards. Geostand Geoanalyt Res 29:333–338. https://doi.org/10.1111/j.1751-908X.2005.tb00904.x

Jochum KP, Weis U, Schwager B, et al (2016) Reference values following ISO guidelines for frequently requested rock reference materials. Geostand Geoanal Res 40:333–350. https://doi.org/10.1111/j.1751-908X.2015.00392.x

Jochum KP, Willbold M, Raczek I, et al (2005b) Chemical characterisation of the USGS reference glasses GSA-1G, GSC-1G, GSD-1G, GSE-1G, BCR-2G, BHVO-2G and BIR-1G using EPMA, ID-TIMS, ID-ICP-MS and LA-ICP-MS. Geostand Geoanalyt Res 29:285–302. https://doi.org/10.1111/j.1751-908X.2005.tb00901.x

Jollands MC, O'Neill HStC, Van Orman J, et al (2018) Substitution and diffusion of Cr2+ and Cr3+ in synthetic forsterite and natural olivine at 1200–1500 °C and 1 bar. Geochimica et Cosmochimica Acta 220:407–428. https://doi.org/10.1016/j.gca.2017.09.030

Laubier M, Grove TL, Langmuir CH (2014) Trace element mineral/melt partitioning for basaltic and basaltic andesitic melts: An experimental and laser ICP-MS study with application to

the oxidation state of mantle source regions. Earth and Planetary Science Letters 392:265–278. https://doi.org/10.1016/j.epsl.2014.01.053

Le Voyer M, Hauri EH, Cottrell E, et al (2019) Carbon Fluxes and Primary Magma CO2 Contents Along the Global Mid-Ocean Ridge System. Geochem Geophys Geosyst 20:1387–1424. https://doi.org/10.1029/2018GC007630

Sun C (2018) Partitioning and Partition Coefficients. In: Bobrowsky P, Marker B (eds) Encyclopedia of Engineering Geology. Springer International Publishing, Cham, pp 1–2

Sun C, Liang Y (2014) An assessment of subsolidus re-equilibration on REE distribution among mantle minerals olivine, orthopyroxene, clinopyroxene, and garnet in peridotites. Chemical Geology 372:80–91. https://doi.org/10.1016/j.chemgeo.2014.02.014

Sylvester PJ (2008) Matrix Effects in Laser Ablation-ICPMS. In: Laser ablation–icp–ms in the earth sciences current practices and outstanding issues. Mineralogical Association of Canada Short Course Series, pp 67–78

Voigt M, von der Handt A (2011) Influence of subsolidus processes on the chromium number in spinel in ultramafic rocks. Contrib Mineral Petrol 162:675–689. https://doi.org/10.1007/s00410-011-0618-3

Wan Z, Coogan LA, Canil D (2008) Experimental calibration of aluminum partitioning between olivine and spinel as a geothermometer. American Mineralogist 93:1142–1147. https://doi.org/10.2138/am.2008.2758

Witt-Eickschen G, O'Neill HStC (2005) The effect of temperature on the equilibrium distribution of trace elements between clinopyroxene, orthopyroxene, olivine and spinel in upper mantle peridotite. Chemical Geology 221:65–101. https://doi.org/10.1016/j.chemgeo.2005.04.005

Witt-Eickschen G, Palme H, O'Neill HStC, Allen CM (2009) The geochemistry of the volatile trace elements As, Cd, Ga, In and Sn in the Earth's mantle: New evidence from in situ analyses of mantle xenoliths. Geochimica et Cosmochimica Acta 73:1755–1778. https://doi.org/10.1016/j.gca.2008.12.013

Workman RK, Hart SR (2005) Major and trace element composition of the depleted MORB mantle (DMM). Earth and Planetary Science Letters 231:53–72. https://doi.org/10.1016/j.epsl.2004.12.005

Yamada N (2015) Kinetic energy discrimination in collision / reaction cell ICP-MS : Theoretical review of principles and limitations. Spectrochimica Acta Part B: Atomic Spectroscopy 110:31–44. https://doi.org/10.1016/j.sab.2015.05.008

Yao L (2015) Closure Temperature and Closure Pressure in Bi-Mineralic Systems with Applications to REE-in-Two-Mineral Thermobarometers. Brown University